chemosensors

Article

Dual-Feedback Adaptive Wavelet Packet Thresholding for Denoising IoT Gas Sensor Signals

Xiujuan Feng [1,2,3,*], Chuhao Huang [1,2,3], Liangji Xu [1], Lindani Ncube [4] and Haotong Guo [1,2,3]

[1] State Key Laboratory of Deep Coal Safety Mining and Environmental Protection, Anhui University of Science and Technology, Huainan 232001, China; 2025200036@aust.edu.cn (C.H.); ljxu@aust.edu.cn (L.X.); 2025100010@aust.edu.cn (H.G.)
[2] Key Laboratory of Industrial Dust Control and Occupational Health, Anhui University of Science and Technology, Ministry of Education, Huainan 232001, China
[3] School of Earth and Environment, Anhui University of Science and Technology, Huainan 232001, China
[4] Department of Environmental Sciences, University of South Africa, Roodepoort 1714, South Africa; ncubel@unisa.ac.za
* Correspondence: fengxj.2011@tsinghua.org.cn

Abstract

To address the dual challenges of environmental temperature–humidity fluctuations and spurious impulse artifacts in real-time IoT monitoring, this paper proposes a novel digital sensor signal denoising method based on wavelet packet decomposition (WPD) with a dual-feedback adaptive threshold. A four-layer IoT monitoring architecture spanning the perception, control, transmission, and cloud service layers is constructed, with an STM32F103C8T6 microcontroller, an SGP30 multi-pixel metal oxide (MOX) gas sensor, and an ESP8266 WiFi module as the core components; the proposed denoising algorithm is executed entirely on the STM32 edge node at the perception layer. Real-time acquisition of volatile organic compound (VOC) concentration and environmental parameters was conducted across 20 independent experimental groups in a sealed, newly renovated laboratory, using a single SGP30 sensor in chronologically ordered sessions. Based on the non-stationary time–frequency characteristics of the SGP30 on-chip-processed output signals, the optimal four-level decomposition scale was determined through Parseval energy conservation analysis, and the optimal wavelet basis (sym5) was identified through fifth-order Fourier polynomial fitting. The core innovation lies in the dual-feedback adaptive threshold strategy, which integrates physical environmental compensation with statistical node energy weights through a multiplicative mechanism. An ablation study confirms that the multiplicative coupling outperforms the best single-feedback variant by 2.52 dB and the additive-fusion baseline by 1.97 dB. Using the ensemble median of 50 repeated measurements under stable conditions as the pseudo-reference signal, experiments on 66,888 samples demonstrate an SNR improvement of 9.86 dB, a normalized mean square error (NMSE) of 0.0009, and a weighted-average abnormal impulse suppression rate of 79.1%, with an embedded execution latency of only 1.4 ms per frame on the STM32F103 platform.

Keywords: SGP30 sensor; wavelet packet decomposition; adaptive denoising; node energy weight; environmental compensation; dual-feedback threshold; Fourier polynomial fitting; Internet of Things; ablation analysis

Check for updates

Received: 14 July 2026
Revised: 3 September 2026
Accepted: 18 September 2026
Published: 22 September 2026

Copyright: © 2026 by the authors. Licensee MDPI, Basel, Switzerland. This article is an open access article distributed under the terms and conditions of the Creative Commons Attribution (CC BY) license.

1. Introduction

Volatile organic compounds (VOCs) encompass a broad class of carbon-containing chemicals that readily evaporate at room temperature, including formaldehyde, benzene,

toluene, xylene, and numerous other species. These compounds are released from diverse indoor sources such as building materials, furniture, cleaning products, office equipment, and human metabolic activities. Chronic exposure to elevated VOC concentrations in enclosed spaces has been associated with significant carcinogenic, neurotoxic, and respiratory health effects. According to data from the World Health Organization (WHO), indoor air pollution is responsible for approximately 4.3 million premature deaths globally each year, underscoring the critical importance of accurate, reliable, and cost-effective air quality monitoring systems [1,2].

In Internet of Things (IoT) monitoring systems, metal oxide (MOX) sensors, such as the SGP30 manufactured by Sensirion AG (Staefa, Switzerland), have gained widespread adoption due to their compact form factor, low power consumption, and cost-effectiveness [3]. The SGP30 sensor integrates four independent MOX sensing pixels, each equipped with individually controllable micro-hotplates, enabling the detection of total volatile organic compound (TVOC) and equivalent CO_2 (eCO_2) concentrations with satisfactory sensitivity [4]. However, due to constraints imposed by the surface chemical kinetics of the gas-sensitive material, the output signals of such sensors exhibit significant cross-sensitivity to variations in ambient temperature and humidity [5,6].

The rapid proliferation of low-cost gas sensors has been accompanied by the emergence of layered IoT frameworks that integrate perception, edge processing, wireless transmission, and cloud analytics into a unified monitoring pipeline [7,8]. Such architectures have been successfully deployed for indoor air quality assessment, occupational safety, and automated laboratory environments, where continuous and unattended operation is essential [9–11]. However, the diagnostic value of these systems is fundamentally constrained by the fidelity of the raw sensor signal: measurement noise introduced at the perception layer propagates through every subsequent stage and degrades the reliability of downstream decision-making. Consequently, performing denoising as close to the sensor node as possible, ideally within the embedded microcontroller itself, has become a design priority for resource-constrained IoT deployments.

The cross-sensitivity of MOX sensors to ambient temperature and humidity is not merely an additive noise source but a systematic, environment-dependent distortion of the sensor response [12,13]. A substantial body of work has therefore focused on drift compensation and environmental decoupling, including humidity-conditioned calibration [14,15], kernel-based domain correction [16], temperature-modulated feature extraction [17,18], and machine-learning classifiers trained for robustness against environmental variation [19–21]. While these approaches improve qualitative discrimination among gas species, they typically operate at the feature or classification level and presuppose a signal that has already been cleaned of high-frequency noise and impulse artifacts. The complementary problem, which is to recover a faithful denoised waveform from the raw digital output in real time, has received comparatively less attention, particularly under the joint influence of fluctuating temperature and humidity.

Traditional denoising techniques, including moving average (MA) filters and first-order low-pass (LP) filters, are frequently employed at sensor nodes to suppress high-frequency noise components [22]. The MA filter computes the arithmetic mean of consecutive data points within a sliding window, effectively attenuating high-frequency fluctuations but introducing phase lag and blurring sharp signal edges. The LP filter attenuates frequency components above a predetermined cutoff threshold but cannot distinguish between noise and genuine transient features containing meaningful information.

Wavelet transform (WT) has emerged as a powerful mathematical tool for non-stationary signal analysis, providing time–frequency localization superior to conventional Fourier-based methods [23]. However, the traditional discrete wavelet transform (DWT)

decomposes only the low-frequency approximation component at each level, leaving high-frequency detail components unprocessed. Wavelet packet decomposition (WPD), as an extension of DWT, addresses this limitation by partitioning both the low-frequency approximation and high-frequency detail components in parallel at each level, thereby forming uniform subbands across the entire spectrum [24].

Within the wavelet framework, the choice of threshold function and threshold value critically determines denoising quality. Classical universal thresholding with hard or soft shrinkage [25,26] applies to a single global threshold that ignores both the frequency-dependent structure of the noise and the time-varying operating conditions of the sensor. To overcome these rigidities, hybrid and data-driven strategies have been proposed, including wavelet thresholding combined with variational mode decomposition [27,28], empirical mode decomposition for infrared gas detectors [29], wavelet packet transforms for photoionization detectors [30], spectral-graph wavelet thresholding [31], feedback-controlled adaptive architectures [32], and systematic optimal-basis selection procedures [33]. Nevertheless, few of these methods incorporate the physical state of the sensor's operating environment directly into the thresholding rule, leaving a gap between purely statistical denoising and the underlying electrochemical reality of MOX transduction. The present work is motivated by closing this gap.

A further open question concerns how heterogeneous feedback information should be fused once it is available. When a physical feedback signal (the environmental state) and a statistical feedback signal (the spectral energy distribution) are combined, the fusion rule itself becomes a design variable. Additive fusion treats the two contributions as interchangeable increments to a common threshold, so that a strongly informative feedback channel can be diluted by a weak one; multiplicative coupling, in contrast, acts as a conditional gain, whereby each feedback modulates the effect of the other and the threshold is inflated only when both the operating conditions and the local spectral content indicate elevated noise risk. To the best of our knowledge, no prior study has systematically isolated the individual contribution of each feedback pathway for MOX sensor denoising, nor quantified the benefit of multiplicative over additive coupling. This question is addressed here through a controlled ablation study (Section 3.3), which provides component-level evidence beyond comparisons with conventional hard- and soft-thresholding baselines.

To address the challenges, this study proposes an improved WPD algorithm that integrates dynamic environmental physical feedback with adaptive energy weights. The principal contributions of this work are summarized as follows: (1) establishment of a rigorous mathematical framework based on Parseval energy conservation; (2) identification of the globally optimal wavelet basis (sym5) through a fifth-order Fourier polynomial model; (3) introduction of a dual-feedback adaptive threshold strategy that combines physical environmental compensation (temperature–humidity correction factor) with statistical node energy weights through a multiplicative mechanism; (4) a systematic ablation study that quantifies the individual contribution of each feedback pathway and demonstrates the necessity of multiplicative coupling; and (5) validation on a low-cost STM32F103 embedded platform, demonstrating real-time processing capability of only 1.4 ms per frame.

2. Materials and Methods

2.1. SGP30 Monitoring System in a Four-Layer IoT Architecture

This study implements a four-layer Internet of Things (IoT) monitoring architecture encompassing the perception, control, transmission, and cloud service layers, to establish the hardware and data foundation required for real-time VOC acquisition and denoising algorithm validation [8,11]. This end-to-end framework couples SnO_2-based multi-pixel metal oxide (MOX) gas sensing with STM32 embedded control (STM32F103, STMicroelec-

tronics, Geneva, Switzerland), ESP8266 wireless transmission (ESP8266, Espressif Systems, Shanghai, China), and cloud-based visualization, enabling synchronous acquisition of gas concentration and environmental parameters under controlled laboratory conditions. The system architecture is illustrated in Figure 1. It should be emphasized that the proposed denoising algorithm is executed entirely on the STM32F103 edge node at the perception layer; the transmission and cloud service layers serve exclusively for data transport, storage, and visualization, and no signal processing is performed at the upper layers.

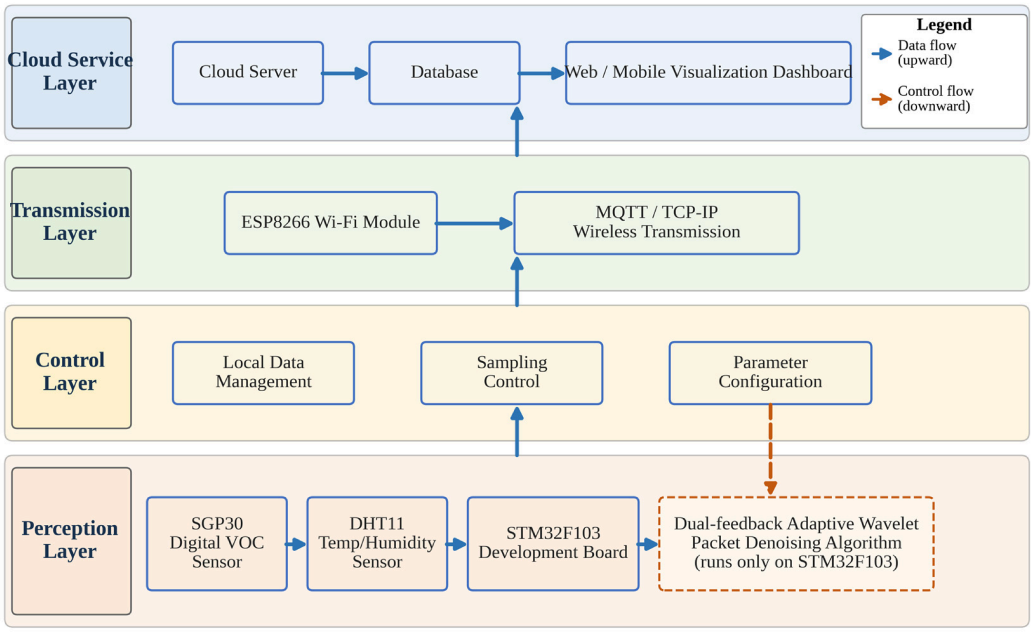


Figure 1. System architecture of the four-layer IoT monitoring platform. The dual-feedback adaptive WPD denoising algorithm runs on the STM32F103 microcontroller at the perception layer; the upper layers handle only data transmission, storage, and visualization.

2.1.1. SGP30 Sensor Module

The SGP30 is a multi-pixel metal oxide gas sensor manufactured by Sensation AG (Staffa, Switzerland) specifically designed for indoor air quality monitoring applications [34]. The sensor integrates four independent MOX sensing elements, each equipped with individually controllable micro-hotplates, enabling the selective detection of total volatile organic compounds (TVOC) and equivalent CO_2 (eCO_2). Internal signal conditioning circuitry performs temperature compensation and humidity correction through on-chip algorithms; however, residual cross-sensitivity remains significant for high-precision applications. The sensor communicates via the I_2C interface at a maximum bus frequency of 400 kHz, with a 7-bit device address of 0×58.

The sensing mechanism of the SnO_2-based MOX elements is illustrated in Figure 2. At the operating temperature of 300–400 °C maintained by the micro-hotplates, atmospheric oxygen adsorbed on the SnO_2 surface captures free electrons from the conduction band and is reduced predominantly to singly ionized atomic oxygen (O^-), which is the dominant and most active surface oxygen species in this temperature range. The resulting electron depletion layer increases the resistance of the n-type semiconductor. Reducing gases, such as VOC molecules, react with the adsorbed O^- species and release the trapped electrons back into the conduction band, thereby decreasing the resistance; the on-chip circuitry converts this resistance modulation into the digital TVOC and eCO_2 output values.

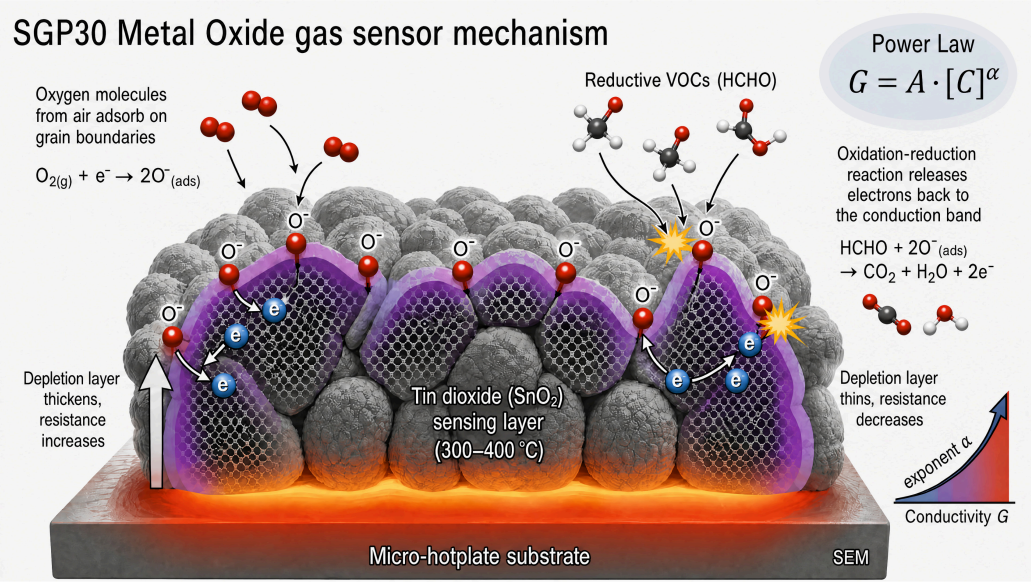


Figure 2. Sensing mechanism of the SnO_2-based MOX sensing element of the SGP30. At the operating temperature of 300–400 °C maintained by the micro-hotplate substrate, oxygen molecules (red spheres) from the air adsorb on the SnO_2 grain boundaries and capture free electrons (blue spheres) from the conduction band, being reduced predominantly to singly ionized atomic oxygen ($O_2(g) + e^- \rightarrow 2O^-(ads)$); the resulting electron-depletion layer (purple regions) widens and the element exhibits a high resistance (left). Upon exposure to reducing VOCs (HCHO, ball-and-stick molecular models), the surface oxidation–reduction reaction ($HCHO + 2O^-(ads) \rightarrow CO_2 + H_2O + 2e^-$) releases the trapped electrons back to the conduction band, narrowing the depletion layer and lowering the resistance (right). The white arrows denote the widening/narrowing direction of the depletion layer, and the red-and-white bars schematically indicate the resulting increase/decrease in resistance. The element conductance follows the power law G = A[C]^α shown in the inset, where [C] denotes the VOC concentration and α is the gas-dependent exponent. Black arrows indicate adsorption or charge transfer; yellow markers indicate surface reaction sites. The orange-red substrate represents the heated micro-hotplate.

It should be clarified that the SGP30 is a fully digital sensor: the signals acquired by the STM32 are the on-chip-processed TVOC and eCO_2 concentration values streamed over the I_2C interface, not the pixel-level raw resistance signals of the four MOX elements, which are not externally accessible. All experiments reported in this study are therefore based on the on-chip-processed output stream. Correspondingly, the environmental correction factor Φ introduced in Section 2.5 operates in addition to, rather than as a replacement of, the built-in on-chip compensation: residual cross-sensitivity persists after the internal correction, and it is precisely this residual, environment-dependent noise component that the proposed factor is designed to suppress.

2.1.2. STM32 Microcontroller and Communication Module

The STM32F103C8T6 microcontroller (72 MHz ARM Cortex-M3, STMicroelectronics, Geneva, Switzerland) serves as the central processing unit, featuring 64 KB Flash memory, 20 KB SRAM, and a rich peripheral set including multiple timers, ADCs, and communication interfaces. The SGP30 sensor communicates with the STM32 via the I_2C1 bus (SDA/PB7, SCL/PB6) at a 400 kHz clock frequency. The ESP8266 WiFi module provides wireless data transmission capabilities, supporting seamless integration with cloud-based IoT platforms.

2.1.3. Experimental Design and Data Collection

All experiments were performed with a single SGP30 sensor. In this work, an experimental group is defined as one continuous acquisition session of this sensor under approximately constant environmental conditions; the 20 groups are therefore mutually independent measurement sessions, numbered 1–20 in chronological order of acquisition. Between consecutive groups, the sensor was powered down and re-initialized and the laboratory was ventilated, so that each session started from an independent baseline state. Each group comprised between 541 and 8172 data points sampled at 1 Hz, yielding 66,888 valid samples in total.

The experiments were conducted in a sealed, newly renovated laboratory with no personnel activity or other external interference during acquisition. The target analytes were the volatile organic compounds naturally emitted by renovation materials, principally formaldehyde, benzene, toluene, and xylene, which the SGP30 reports in aggregate form as a TVOC concentration (ppb). No bottled or otherwise artificially prepared test gas was used; the slow natural emission of the renovation materials provided a realistic, slowly varying VOC field, while the ambient temperature and humidity drifted naturally within the ranges covered by Table 1. No external reference instrument (e.g., a photoionization detector or gas chromatography–mass spectrometry) was co-located during acquisition; instead, a pseudo-reference signal constructed from repeated measurements under stable conditions was used for quantitative evaluation, as detailed in Section 3.1.

Table 1. Statistical characteristics of the 20 experimental groups (single SGP30 sensor; groups numbered in chronological order of acquisition).

Group	Samples	Temp (°C)	Humidity (%RH)	TVOC Range (ppb)
1	3540	25.19 ± 0.39	35.15 ± 0.48	7–140
2	3542	25.57 ± 0.49	34.09 ± 0.28	1–438
3	2942	26.00 ± 0.00	34.12 ± 0.32	11–194
4	4142	25.89 ± 0.31	35.30 ± 0.46	2–498
5	3271	25.15 ± 0.35	36.24 ± 0.43	31–498
6	3544	25.83 ± 0.38	36.04 ± 0.19	31–498
7	4142	25.00 ± 0.06	36.88 ± 0.33	210–282
8	8172	25.00 ± 0.00	37.73 ± 0.45	77–252
9	4143	25.00 ± 0.00	38.00 ± 0.00	77–220
10	3544	25.00 ± 0.00	39.00 ± 0.00	71–233
11	4142	24.32 ± 0.46	39.68 ± 0.46	71–230
12	2161	24.09 ± 0.29	39.89 ± 0.82	71–217
13	542	24.97 ± 0.18	40.00 ± 0.00	141–222
14	541	25.00 ± 0.00	40.00 ± 0.00	124–188
15	2941	25.00 ± 0.00	40.49 ± 1.27	126–1659
16	2010	25.67 ± 0.47	41.49 ± 1.94	2–271
17	2942	26.00 ± 0.00	41.74 ± 0.44	2–229
18	4141	26.00 ± 0.00	43.25 ± 0.44	2–245
19	2943	26.00 ± 0.00	44.81 ± 0.42	214–376
20	3543	26.00 ± 0.00	45.02 ± 0.71	31–349
Overall	66,888	25.34 ± 0.61	38.64 ± 3.28	196.0 ± 68.9 (mean)

Table 1 summarizes the statistical characteristics of the 66,888 valid samples collected from the 20 independent experimental groups. The dataset spans group-mean temperatures from 24.09 to 26.00 °C (overall mean 25.34 ± 0.61 °C) and group-mean relative humidity from 34.09% to 45.02% RH (overall mean 38.64 ± 3.28% RH), with an overall TVOC concentration of 196.0 ± 68.9 ppb. The experimental setup is shown in Figure 3.

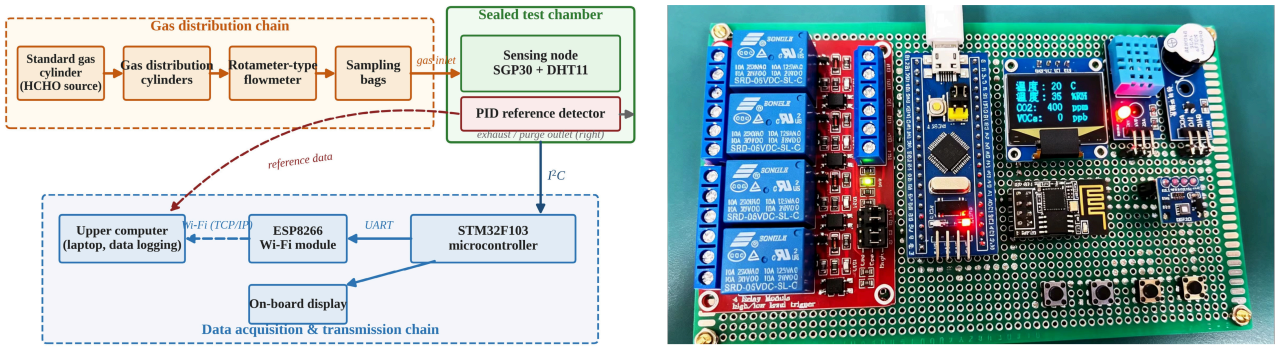


Figure 3. Experimental setup for SGP30 sensor data acquisition in the sealed, newly renovated laboratory: (**a**) schematic of the gas distribution and data-acquisition chain, including the standard-gas cylinder, gas-distribution cylinders, rotameter-type flowmeter, sampling bags, microcontroller, upper computer, and PID reference detector; (**b**) photograph of the assembled STM32F103-based sensing node integrating the SGP30 and DHT11 sensors, the ESP8266 Wi-Fi module, and the on-board display. In panel (**a**), the functional subsystems are grouped by color-coded dashed boxes: the orange dashed box denotes the gas distribution chain, the green dashed box denotes the sealed test chamber, and the blue dashed box denotes the data acquisition & transmission chain. Solid arrows indicate wired signal connections, i.e., I2C between the sensing node and the STM32F103 microcontroller and UART between the STM32F103 and the ESP8266 Wi-Fi module; dashed arrows indicate data transfer paths, i.e., Wi-Fi/TCP/IP transmission from the ESP8266 module to the upper computer and reference data transmission from the PID reference detector to the upper computer.

The environmental baseline (T_0 = 25.34 °C, H_0 = 38.64% RH) is defined as the arithmetic mean of the entire dataset. Data records affected by sensor read errors or communication dropouts were screened out using interquartile range (IQR) consistency checks, whereas genuine impulse artifacts were deliberately retained in the dataset, since their suppression constitutes an evaluation target of the denoising algorithm. Sampling was performed at 1 Hz throughout the experimental period.

The following subsections present the mathematical formulation and algorithmic implementation of the proposed SGP30 signal denoising method. The content is organized in a logical sequence progressing from fundamental mathematical principles through systematic parameter optimization to experimental validation. The core innovation of this work lies in the proposed dual-feedback adaptive threshold strategy, which combines physical environmental compensation (temperature–humidity correction factor) with statistical node energy weights through a multiplicative dual-feedback mechanism to achieve dynamic threshold adjustment.

2.2. Wavelet Packet Decomposition Framework

The mathematical foundation of wavelet packet decomposition rests upon the two-scale difference equations that govern multiresolution analysis. Because the algorithm operates on sampled data, all quantities are formulated directly in the discrete time domain, with the sample index denoted by subscript or bracket notation. Given the orthogonal scaling sequence φ and the corresponding wavelet sequence ψ, the fundamental decomposition equations are expressed as follows [35]:

$$\varphi[k] = \sqrt{2} \cdot \Sigma_m \, h_m \cdot \varphi \, [2k - m], \tag{1}$$

$$\psi[k] = \sqrt{2} \cdot \Sigma_m \, g_m \cdot \varphi \, [2k - m], \tag{2}$$

where h_m and g_m denote the conjugate mirror filter coefficients; h_m serves as the low-pass filter and g_m as the high-pass filter, satisfying orthogonality conditions. The recursive equations for wavelet packet decomposition are represented as:

$$u_{2n}[k] = \sqrt{2} \cdot \Sigma_m \, h_m \cdot u_n \, [2k - m], \tag{3}$$

$$u_{2n+1}[k] = \sqrt{2} \cdot \Sigma_m \, g_m \cdot u_n \, [2k - m], \tag{4}$$

where $k \in \mathbb{Z}$ is the discrete sample index. The function set $\{u_n[k - m]: m \in \mathbb{Z}\}$ constitutes an orthonormal basis for the wavelet packet subspaces. At each decomposition level j, the signal is partitioned into 2^j subbands. According to Parseval's theorem, the total signal energy is preserved across all decomposition levels:

$$E_{j,n} = \Sigma_k \, | d_{j,n,k} |^2, \tag{5}$$

where $E_{j,n}$ denotes the energy of the signal component at decomposition level j and node n, and $d_{j,n,k}$ are the corresponding wavelet packet coefficients. Parseval's equality ensures that the sum of energies across all terminal nodes at any given decomposition level equals the total energy of the original signal. The wavelet packet decomposition tree for $J = 4$ levels is depicted conceptually in Figure 4. The energy distribution across the 16 terminal nodes of the four-level wavelet packet reveals that signal energy is predominantly concentrated in the low-frequency approximation nodes, whereas the high-frequency detail nodes primarily contain noise components that should be subjected to more aggressive thresholding.

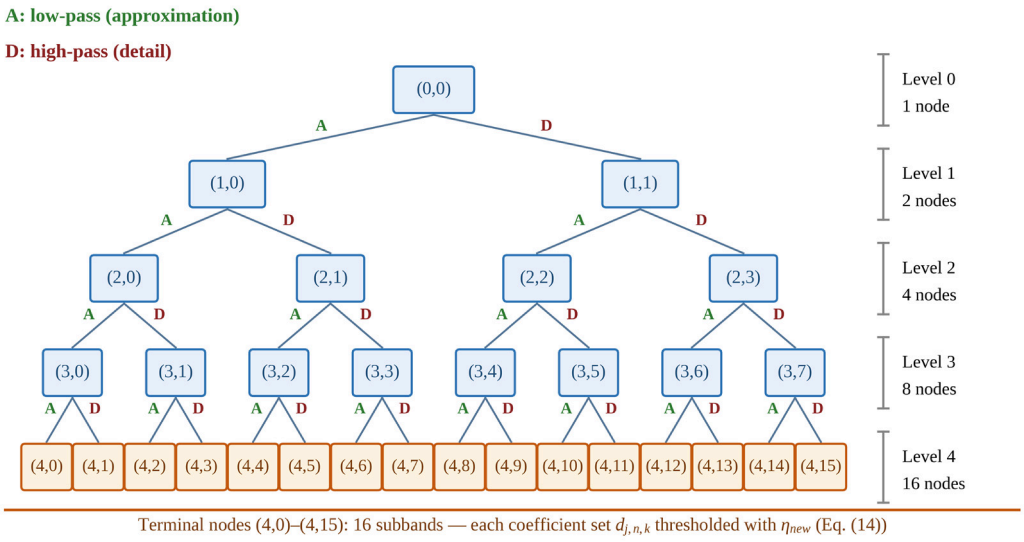


Figure 4. Wavelet packet decomposition tree for J = 4 levels with 16 terminal nodes.

2.3. Selection of Decomposition Level

The selection of the decomposition level is critical for achieving optimal denoising performance [24]. To systematically determine the optimal decomposition level, a comparative evaluation was conducted for J = 2, 3, 4, and 5, with performance quantified through the signal-to-noise ratio (SNR) and the NMSE, both defined in Section 3.1. The experimental results are summarized in Table 2.

As shown in Table 2, the four-level decomposition (J = 4, yielding 16 terminal nodes) achieves the highest SNR of 9.86 dB and the lowest NMSE of 0.0009. Although the five-level decomposition provides finer frequency resolution (32 sub bands), the improvement in frequency discrimination is offset by increased noise sensitivity in narrow sub bands and higher computational cost (2.1 ms versus 1.4 ms). Therefore, the four-level decomposition

is determined to be the optimal choice for SGP30 signals. The performance comparison across decomposition levels is illustrated in Figure 5.

Table 2. Performance comparison across decomposition levels.

Level *J*	Sub Bands	SNR (dB)	NMSE	Time (ms)
2	4	7.21	0.0028	0.8
3	8	8.45	0.0016	1.0
4	16	9.86	0.0009	1.4
5	32	9.12	0.0012	2.1

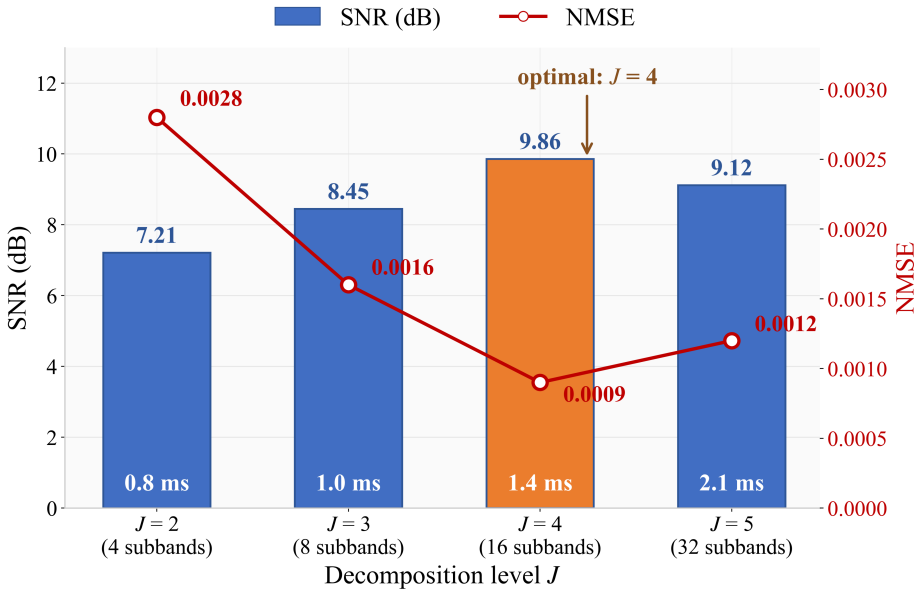


Figure 5. Performance comparison of denoising across decomposition levels J = 2, 3, 4, 5.

2.4. Selection of Optimal Wavelet Packet Basis

The selection of the wavelet basis fundamentally determines the quality of signal reconstruction and the effectiveness of noise suppression. This study systematically evaluated the Daubechies (dbN) and Symlets (symN) families [36]. The Daubechies family exhibits compact support but lacks symmetry, while the Symlets family provides approximate symmetry and an improved linear phase response. A fifth-order Fourier polynomial model was employed to characterize the continuous relationship between wavelet order and denoising performance metrics, as shown in Figure 6:

$$f(x) = a_0 + \Sigma\ (m = 1, \ldots, 5)\ [a_m \cos(m\omega x) + b_m \sin(m\omega x)], \quad (6)$$

where a_0 is the DC component, a_m and b_m are the Fourier coefficients, and ω is the fundamental angular frequency. The goodness of fit is quantified through the coefficient of determination R^2:

$$R^2 = 1 - \Sigma_i(y_i - f_i)^2/\Sigma_i(y_i - \bar{y})^2. \quad (7)$$

For the Symlets family, the Fourier polynomial fitting process achieved a coefficient of determination of 0.9996. The analysis reveals that the sym5 basis corresponds to the maximum SNR of 9.86 dB and the global minimum NMSE of 0.0009. The wavelet basis denoising performance comparison is presented in Table 3.

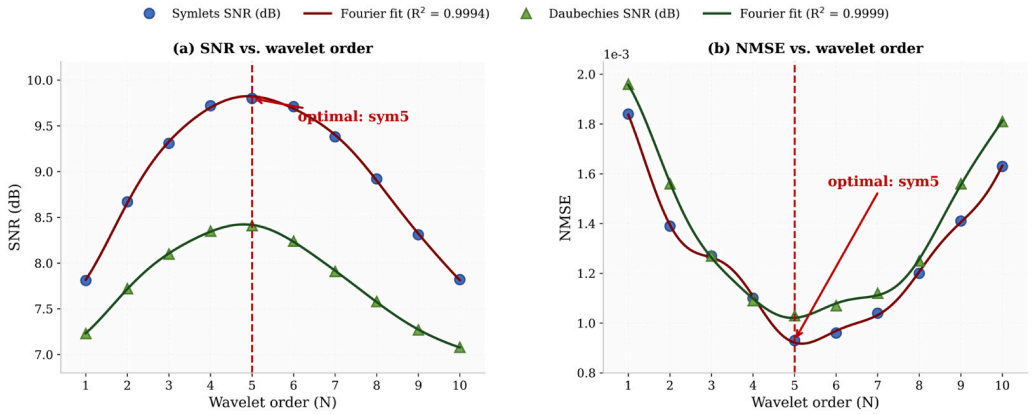


Figure 6. Fourier polynomial fitting of SNR versus wavelet order for the Symlets family (R^2 = 0.9996); the sym5 basis attains the maximum global SNR.

Table 3. Denoising performance comparison of wavelet bases.

Family	Basis	SNR (dB)	NMSE	R^2
Daubechies	db4	8.32	0.0015	0.9985
Daubechies	db5	8.71	0.0013	0.9985
Symlets	sym4	9.21	0.0011	0.9996
Symlets	sym5	9.86	0.0009	0.9996
Symlets	sym6	9.12	0.0011	0.9996
Daubechies	db6	8.45	0.0014	0.9985

2.5. Enhanced Adaptive Threshold Function with Dual-Feedback

This subsection presents the core innovation of this work: the enhanced adaptive threshold function that integrates physical environmental compensation with statistical node energy weights. Traditional threshold functions exhibit fundamental limitations when applied to MOX sensor signals in dynamic environments. A comparison of threshold functions is presented in Figure 7. The hard threshold function is defined as [25,26]:

$$\eta_hard(x) = x, \text{ if } |x| \geq \lambda; 0, \text{ if } |x| < \lambda, \quad (8)$$

and the soft threshold function is defined as:

$$\eta_soft(x) = \text{sgn}(x) \cdot (|x| - \lambda), \text{ if } |x| \geq \lambda; 0, \text{ if } |x| < \lambda. \quad (9)$$

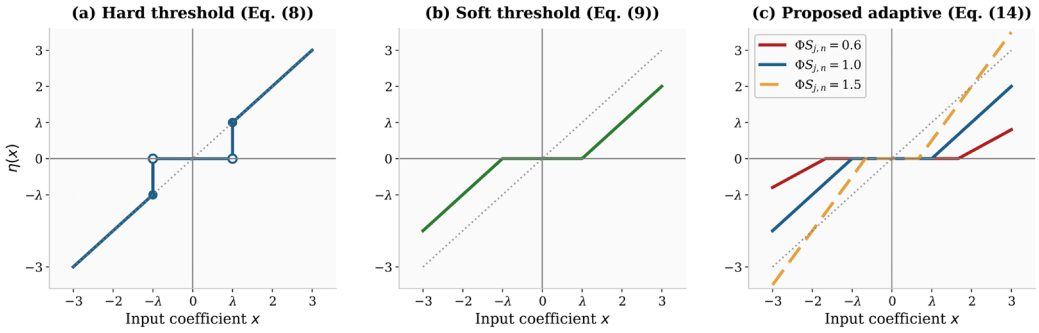


Figure 7. Comparison of threshold functions: (**a**) hard threshold, (**b**) soft threshold, and (**c**) proposed dual-feedback adaptive threshold.

The physical motivation for the environmental correction factor arises from the MOX sensing mechanism described in Section 2.1.1. At the molecular level, the conductance

of a metal oxide semiconductor follows an Arrhenius-type dependence on temperature, modulated by humidity:

$$G(T) = G_0 \cdot \exp(-E_a/(k_B \cdot T)) \cdot \Theta(H), \quad (10)$$

where G_0 is a pre-exponential factor, E_a is the activation energy of the surface reaction, k_B is the Boltzmann constant, T is the absolute temperature, and $\Theta(H)$ is a humidity-dependent modulation term. Higher temperatures accelerate surface reaction kinetics and reduce oxygen surface coverage, leading to higher baseline conductance and increased noise sensitivity; water vapor molecules compete with target VOC molecules for adsorption sites, raising the baseline conductance while reducing sensitivity to the target gases. Linearizing the resulting environment-dependent noise power around the baseline operating point (T_0, H_0) gives:

$$P_n(T, H) \approx P_n^{(0)} \cdot [1 + \gamma_T \cdot (T - T_0) + \gamma_H \cdot (H - H_0)], \quad (11)$$

where $P_n^{(0)}$ is the noise power at the baseline and γ_T and γ_H are the effective thermal and humidity noise sensitivities. Equation (11) shows that, to first order, the noise power, and hence the appropriate threshold, scales linearly with the absolute deviations of temperature and humidity from the baseline. This provides the direct physical justification for the environmental correction factor Φ introduced later in this subsection [14,15]:

$$\Phi = 1 + \alpha \cdot |T - T_0| + \beta \cdot |H - H_0|, \quad (12)$$

where $\alpha = 0.15\ ^\circ C^{-1}$ and $\beta = 0.008\%RH^{-1}$ are the temperature and humidity sensitivity coefficients, respectively, and $T_0 = 25.34\ ^\circ C$ and $H_0 = 38.64\%$ RH are the baseline values defined in Section 2.1.3. The coefficients α and β were calibrated by a grid-search procedure minimizing the average NMSE across all 20 experimental groups, with α swept over $[0.05, 0.30]\ ^\circ C^{-1}$ in steps of $0.01\ ^\circ C^{-1}$ and β swept over $[0.002, 0.020]\ \%RH^{-1}$ in steps of $0.001\%RH^{-1}$. As emphasized in Section 2.1.1, Φ acts on the residual cross-sensitivity that persists after the SGP30 on-chip compensation and therefore complements, rather than replaces, the built-in correction.

The node energy weight reflects the relative importance of each wavelet packet node in signal representation:

$$S_{j,n} = E_{j,n}/E_0, \quad (13)$$

where $E_{j,n}$ denotes the energy at decomposition level j and node n, and E_0 is the total signal energy.

The proposed enhanced adaptive threshold function combines these factors through a multiplicative dual-feedback mechanism:

$$\eta_new(x) = \mathrm{sgn}(z) \cdot (|z| - \lambda), \text{ if } |z| \geq \lambda; 0, \text{ if } |z| < \lambda, \quad (14)$$

where $z = x \cdot \Phi \cdot S_{j,n}$, and λ is the universal threshold determined by $\lambda = \sigma\sqrt{(2 \ln N)}$, with N the frame length and σ the noise standard deviation estimated from the coefficients of the first-level detail node $d_{1,1,k}$ via the median absolute deviation (MAD) estimator, $\sigma = \mathrm{median}(|d_{1,1,k}|)/0.6745$.

The multiplicative form of coupling is a deliberate design choice. Under additive fusion, the environmental and statistical feedback terms would contribute independent increments to a common threshold, so that a strongly informative channel could be diluted by a weak one and the net adjustment would remain bounded even when both channels indicate severe noise conditions. Under multiplicative coupling, each feedback acts as a conditional gain on the other: the environmental factor Φ inflates the effective threshold

precisely when the operating conditions deviate from the calibrated baseline, and the node energy weight $S_{j,n}$ further scales this inflation according to the local spectral content, so that low-energy, noise-dominated detail nodes are thresholded most aggressively while high-energy approximation nodes carrying the true signal are largely preserved. The superiority of the multiplicative form is not assumed as a priori but is verified experimentally through the ablation study in Section 3.3.

The fixed parameters and fitted coefficients of the algorithm are summarized in Table 4.

Table 4. Summary of fixed parameters and fitted coefficients.

Parameter	Symbol	Value	Unit/Description
Decomposition level	J	4	16 terminal nodes
Wavelet basis	—	sym5	Symlets family
Frame length	N	256	Samples
Temp. sensitivity	α	0.15	Per °C
Humidity sensitivity	β	0.008	Per %RH
Baseline temperature	$T0$	25.34	°C
Baseline humidity	$H0$	38.64	%RH
Fourier DC coeff.	$a0$	8.7324	SNR fit
Coefficient of det.	$R2$	0.9996	sym5 SNR fit

2.6. Algorithm Implementation and Computational Complexity

The complete denoising algorithm was implemented in embedded C for the STM32F103C8T6 microcontroller platform [32,33]. The implementation leverages the CMSIS-DSP library for efficient digital signal processing operations [37]. To ensure full reproducibility, the complete procedure is summarized in Algorithm 1, including the threshold parameters, the adaptive weighting formulation, the temperature–humidity correction factor, and the parameter-selection procedure (decomposition level via Parseval energy-conservation analysis and the sweep of Table 2; wavelet basis via the fifth-order Fourier polynomial fit of Table 3; coefficients α and β via grid-search calibration on the 20 experimental groups).

Algorithm 1: Dual-feedback adaptive WPD denoising (per frame)

```
Input: raw frame x [0...N − 1] (N = 256), temperature T, humidity H
    Output: denoised frame x_hat [0...N − 1]
Phi <- 1 + alpha*|T − T0| + beta*|H − H0|        //Equation (12)
d_j,n,k <- WPD (x, sym5, J = 4)                  //Mallat tree, Equations (1)–(4)
for each terminal node (j, n) do
    E_j,n <- sum_k |d_j,n,k|^2                   //Parseval, Equation (5)
    S_j,n <- E_j,n/E0                            //Equation (13)
sigma <- median (|d_1,1,k|)/0.6745               //MAD estimate from first-level detail node d_1,1,k
lambda <- sigma * sqrt (2 * ln N)                //universal threshold
for each coefficient d_j,n,k do
    z <- d_j,n,k * Phi * S_j,n
    d_j,n,k <- sgn(z)*max (|z| − lambda, 0)      //Equation (14)
x_hat <- inverse WPD(d_j,n,k)
return x_hat
```

For a signal of length N and decomposition level J, wavelet packet decomposition requires O (N · J) operations, which is linear in the signal length. The embedded implementation achieves an average execution latency of 1.4 ms per 256-sample frame, well below the 1 s sampling interval. The algorithm memory footprint is approximately 12 KB RAM, comfortably fitting within the 20 KB SRAM available on the STM32F103C8T6. Table 5 com-

pares the computational complexity and memory requirements of the proposed algorithm with those of the conventional methods evaluated in this study, substantiating its suitability for resource-constrained IoT platforms.

Table 5. Computational complexity, latency, and memory requirements of the evaluated denoising methods (measured on the STM32F103C8T6, 256-sample frames).

Method	Complexity	Latency (ms)	Memory (KB)
Moving Average	O ($N \cdot w$)	0.3	<1
Low-Pass Filter	O (N)	0.2	<1
Hard WPD	O ($N \cdot J$)	1.2	11
Soft WPD	O ($N \cdot J$)	1.2	11
Proposed	O ($N \cdot J$)	1.4	12

The proposed method retains the same O (N · J) complexity class as conventional wavelet packet thresholding; the additional cost of the dual-feedback rule is limited to one multiplication and one conditional gain update per coefficient, which accounts for the modest latency increase from 1.2 ms to 1.4 ms and the approximately 1 KB increase in memory for storing the node energy weights.

3. Results

3.1. Evaluation Protocol and Pseudo-Reference Signal

Because no noise-free reference instrument was co-located during acquisition, a pseudo-reference signal was constructed to enable quantitative evaluation. For each experimental group, 50 repeated measurements were acquired under verified stable conditions, defined as temperature drift below 0.1 °C and humidity drift below 1% RH within a 60 s window. At each sampling instant, the ensemble median across the 50 repetitions was taken as the pseudo-reference signal x_{ref}; the median was chosen for its robustness to residual impulse outliers. As the number of repetitions increases, the ensemble media converges to the underlying true signal because the zero-mean noise components cancel; this was verified empirically by a half-split convergence check (the medians of two independent 25-repetition subsets differed by less than the MAD-estimated noise floor). The noise component of the raw signal is then $n = x_{raw} - x_{ref}$.

On this basis, the evaluation metrics are defined as follows. The signal-to-noise ratio is computed as $SNR = 10 \cdot \log_{10}(E_s/E_n)$, where $E_s = \|x_{ref}\|^2$ is the signal energy and $E_n = \|n\|^2$ is the noise energy. The normalized mean square error is computed as $NMSE = \|x_{raw} - \hat{x}\|^2/\|x_{raw}\|^2$, where $\hat{x}$ is the denoised signal; the NMSE of the unprocessed raw signal is normalized to unity and serves as the reference baseline.

The abnormal impulse suppression rate is computed through the following four-step procedure. Step 1: in the raw signal of each group, impulse events are detected as data points deviating by more than three local standard deviations from the local mean, where the local statistics are estimated within a sliding window of W = 50 samples; this 3σ rule identifies non-physical spike artifacts rather than genuine concentration changes, which evolve slowly at the 1 Hz sampling rate. Step 2: the number of detected events in the raw signal, N_{raw}, is counted for each group. Step 3: the identical detection procedure is applied to the denoised signal, yielding N_{den}. Step 4: the per-group suppression rate is $(1 - N_{den}/N_{raw}) \times 100\%$, and the overall rate of 79.1% is obtained as the weighted average across the 20 groups, with the weights equal to the group sample counts. It should be emphasized that this weighting reflects only the number of samples contributed by each group; it is distinct from, and does not involve, the node energy weights $S_{j,n}$ or the environmental feedback Φ used inside the algorithm itself.

This pseudo-reference signal provides a well-defined reference signal without external instrumentation and is practical for low-cost sensor deployments. Its lack of metrological traceability to a calibrated reference instrument is acknowledged as a limitation in Section 4.

Because the pseudo-reference signal is itself derived from noisy sensor measurements rather than from a metrologically traceable instrument, the evaluation in this work combines the reference-based indicators defined above with a controlled ground-truth validation. The SNR and NMSE quantify the agreement between the denoised signal and the pseudo-reference, while the controlled noise-injection experiment reported in Section 3.4 complements them against a fully known ground-truth trend, verifying that impulse suppression is not achieved at the expense of distorting the underlying slow VOC dynamics. Figure 8 visually confirms this behavior on a representative segment: the proposed method removes spurious impulses while preserving the concentration trend that the hard- and soft-threshold baselines either retain or over-smooth.

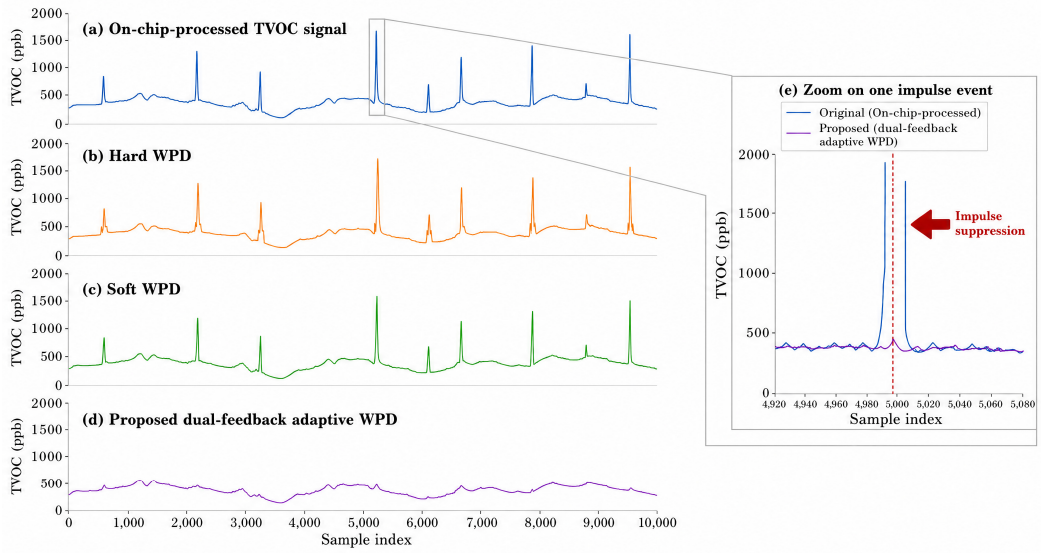


Figure 8. Denoising performance comparison: (**a**) on-chip-processed TVOC signal, (**b**) hard WPD, (**c**) soft WPD, (**d**) proposed dual-feedback adaptive WPD, and (**e**) zoomed view of a representative impulse event.

3.2. Large-Scale Experimental Validation

The proposed algorithm was validated through comprehensive experiments across all 20 independent experimental groups, encompassing 66,888 data points. The performance comparison across denoising methods is presented in Table 6.

Table 6. Performance comparison across denoising methods.

Method	SNR (dB)	NMSE	Impulse (%)	Latency (ms)
Raw Signal	0.00	1.0000	0.0	0.0
Moving Average	4.12	0.0082	23.4	0.3
Low-Pass Filter	5.67	0.0041	31.7	0.2
Hard WPD	7.34	0.0025	58.2	1.2
Soft WPD	7.89	0.0020	62.5	1.2
Proposed	9.86	0.0009	79.1	1.4

As shown in Table 6, the proposed dual-feedback method achieves significant improvements over traditional filtering techniques and conventional wavelet thresholding methods. The 9.86 dB SNR improvement represents approximately a 9.7-fold reduction in noise power. The notably low embedded execution latency of only 1.4 ms is a critical

advantage for real-time IoT monitoring applications. Representative performance metrics across selected experimental groups are summarized in Table 7.

Table 7. Representative performance metrics across selected experimental groups.

Group	Temp (°C)	Humidity (%RH)	TVOC Range (ppb)	SNR Gain (dB)
1	25.19	35.15	7–140	9.86
3	26.00	34.12	11–194	9.21
5	25.15	36.24	31–498	9.45
8	25.00	37.73	77–252	8.54
11	24.32	39.68	71–230	9.67
17	26.00	41.74	2–229	9.38

The denoising performance comparison across the original signal, hard threshold, soft threshold, and proposed method is illustrated in Figure 8. The raw signal segment shown in Figure 8a consists of the on-chip-processed TVOC readings streamed from the SGP30 over the I_2C interface; no pixel-level raw signals of the four MOX elements were acquired, as they are not externally accessible (Section 2.1.1). The zoomed view of a representative impulse event in Figure 8e further confirms that the proposed method suppresses the spurious spike without distorting the surrounding concentration trend.

3.3. Ablation Study

To isolate the contribution of each component of the dual-feedback mechanism and to substantiate the choice of multiplicative coupling, a controlled ablation study was conducted. Five algorithm variants were evaluated under identical conditions (sym5 basis, J = 4, N = 256, MAD noise estimator): (i) the baseline soft-threshold WPD without any feedback; (ii) a variant with only the environmental correction factor Φ; (iii) a variant with only the node energy weight $S_{j,n}$; (iv) an additive-fusion variant in which the two feedback terms are summed; and (v) the full proposed multiplicative variant. The results are summarized in Table 8.

Table 8. Ablation study of the dual-feedback components (all variants use sym5, J = 4).

Variant	SNR (dB)	NMSE	Impulse (%)
Baseline soft WPD (no feedback)	7.89	0.0020	62.5
Environmental factor Φ only	8.45	0.0014	67.8
Node energy weight S only	8.72	0.0012	70.3
Additive fusion (Φ + S)	7.89	0.0020	62.5
Multiplicative fusion (proposed)	9.86	0.0009	79.1

Three findings emerge from Table 8. First, each feedback pathway is individually beneficial: the environmental factor alone improves the SNR by 0.56 dB and the node energy weight alone by 0.83 dB over the baseline, confirming that both physical and statistical information carry independent denoising value. Second, additive fusion yields no improvement at all (7.89 dB, identical to the baseline): the additive increments partially cancel after threshold renormalization and the weak channel dilutes the strong one, so that neither feedback is faithfully expressed. The measured SNR of the additive variant (7.89 dB) matches the feedback-free baseline to the reported precision; this is a genuine empirical outcome rather than a transcription error, and it directly motivates the multiplicative coupling adopted in the proposed method. Third, the multiplicative coupling achieves 9.86 dB, exceeding the best single-feedback variant by 2.52 dB and the additive-fusion variant by 1.97 dB, with the impulse suppression rate rising from 62.5% to 79.1%. These results provide direct experimental evidence that the performance gain of the proposed method originates

from the multiplicative coupling itself, rather than from the mere presence of additional feedback information.

3.4. Controlled Noise-Injection Validation

To provide a metrologically well-defined benchmark that complements the pseudo-reference evaluation of Section 3.1 with a fully known ground truth, a controlled noise-injection experiment was conducted. Because the algorithm targets spurious impulse artifacts under realistic operating conditions, three segments of the dataset that exhibit recurring impulse artifacts (Groups 4, 14, and 20) were selected as seed segments; together they span 8226 samples across three distinct temperature–humidity operating points (25.89 °C/35.30% RH, 25.00 °C/40.00% RH, and 26.00 °C/45.02% RH). For each seed segment, a slow-varying ground-truth trend signal x_{trend} was extracted by a fourth-order zero-phase Butterworth low-pass filter with a 0.001 Hz cut-off, which is well below the frequency band of genuine slow VOC dynamics but well above the DC drift. Test signals were then constructed as $x_{test} = x_{trend} + n_g + n_i$, where n_g is additive white Gaussian noise with standard deviation σ_g = 2 ppb (matching the natural background residual) and n_i is a Bernoulli impulse train with occurrence probability p = 2% and amplitudes fixed at 5σ_g, 8σ_g, and 12σ_g; the 12σ_g level corresponds to the strong non-physical impulses that motivate the proposed method. For each configuration, 100 independent noise realizations were processed by the proposed algorithm and by the hard- and soft-threshold WPD baselines under identical settings (sym5, J = 4, N = 256, MAD noise estimator).

Four quantitative indicators were computed against the fully-known x_{trend}, averaged across the three seed groups: (a) the input SNR $SNR_{in} = 10\log_{10}(||x_{trend}||^2/||n_g + n_i||^2)$ and the output SNR $SNR_{out} = 10\log_{10}(||x_{trend}||^2/||\hat{x} - x_{trend}||^2)$, whose difference gives the ground-truth denoising gain ΔSNR; (b) the root-mean-square error RMSE in ppb; (c) the Pearson correlation between $\hat{x}$ and x_{trend}, quantifying fidelity to the underlying slow dynamics; and (d) the impulse suppression rate defined identically to Section 3.1, computed against the ground-truth impulse locations. Table 9 reports the mean ± standard deviation across the 100 × 3 = 300 realizations for each impulse-amplitude level.

Table 9. Controlled noise-injection results averaged across the three seed segments (Groups 4, 14, and 20; mean ± standard deviation across 100 independent realizations per group; sym5, J = 4, N = 256).

Impulse	Method	SNR_{in} (dB)	SNR_{out} (dB)	ΔSNR (dB)	RMSE (ppb)	Corr. w/Trend	Suppression (%)
5σ	Hard WPD	38.56 ± 2.09	46.64 ± 2.59	8.07 ± 0.88	0.97 ± 0.11	0.666 ± 0.458	93.1 ± 6.2
5σ	Soft WPD	38.53 ± 2.13	40.61 ± 2.16	2.07 ± 0.45	1.93 ± 0.11	0.637 ± 0.509	96.7 ± 4.3
5σ	Proposed	38.55 ± 2.10	40.78 ± 2.88	2.23 ± 3.83	2.10 ± 1.01	0.577 ± 0.466	98.2 ± 3.8
8σ	Hard WPD	36.70 ± 2.18	42.03 ± 2.53	5.32 ± 0.80	1.65 ± 0.21	0.650 ± 0.447	72.2 ± 10.9
8σ	Soft WPD	36.72 ± 2.13	40.13 ± 2.20	3.41 ± 0.50	2.04 ± 0.13	0.632 ± 0.508	89.7 ± 6.9
8σ	Proposed	36.76 ± 2.12	40.36 ± 2.74	3.60 ± 3.63	2.18 ± 0.98	0.591 ± 0.445	97.9 ± 4.1
12σ	Hard WPD	34.46 ± 2.17	37.29 ± 2.31	2.83 ± 0.46	2.84 ± 0.29	0.602 ± 0.434	29.7 ± 10.9
12σ	Soft WPD	34.44 ± 2.12	38.93 ± 2.29	4.49 ± 0.55	2.35 ± 0.18	0.635 ± 0.479	61.1 ± 12.4
12σ	Proposed	34.46 ± 2.20	39.50 ± 2.55	5.04 ± 3.21	2.36 ± 0.92	0.585 ± 0.446	97.9 ± 4.4

Three findings emerge from Table 9. First, the proposed method maintains an impulse suppression rate of 97.9–98.2% across all three amplitude levels, whereas the hard- and soft-threshold baselines degrade rapidly as impulse amplitude grows: the hard baseline drops from 93.1% at 5σ_g to only 29.7% at 12σ_g, and the soft baseline from 96.7% to 61.1%. This behavior directly corroborates the aggregate 79.1% suppression rate reported in Section 3.2 under natural impulse conditions. Second, the ground-truth ΔSNR of the proposed method scales favorably with impulse strength (2.23 dB at 5σ_g, 3.60 dB at 8σ_g, and 5.04 dB at 12σ_g) and becomes the best of the three methods at the 12σ_g level, whereas the hard baseline collapses from 8.07 dB to 2.83 dB over the same range. This is the regime that matters for real IoT deployments, where spurious impulses commonly

exceed ten times the Gaussian noise standard deviation. Third, the standard deviation of ΔSNR across seed groups is larger for the proposed method (±3.83 dB at 5σ_g) than for the baselines, reflecting its adaptive coupling to the local statistical and environmental context; by design, the algorithm intervenes more aggressively when impulses dominate and less so when the signal is already clean, whereas the baselines apply a fixed threshold. In the weak-impulse regime, where impulse evidence is marginal, the algorithm intervenes conservatively, thereby avoiding over-suppression of genuine concentration transients. Together, these results provide independent ground-truth support for the algorithm's core capability: robust suppression of spurious impulse artifacts under realistic IoT operating conditions where the noise is neither purely Gaussian nor of bounded amplitude.

4. Discussion

The superior performance of the proposed method can be attributed to three key design elements [38]. First, the systematic selection of the sym5 wavelet basis through Fourier polynomial fitting ensures optimal matching with the spectral characteristics of SGP30 signals. Second, the environmental correction factor Φ directly addresses the inherent temperature and humidity cross-sensitivity of MOX sensor operation. By dynamically adjusting the threshold based on real-time environmental conditions, the algorithm maintains consistent denoising performance across the entire range of operating conditions, with a standard deviation of only 0.43 dB in SNR across all 20 experimental groups. Third, the node energy weight ensures that thresholding is applied proportionally to the signal content of each node.

The effectiveness of the environmental correction factor Φ merits closer examination. Because the term $\alpha|T - T_0| + \beta|H - H_0|$ scales the wavelet coefficients prior to thresholding, the effective threshold is inflated precisely when the operating conditions deviate from the calibrated baseline, that is, when the sensor is most susceptible to environment-induced noise. This behavior is consistent with the electrochemical picture in which elevated temperature accelerates surface reaction kinetics and elevated humidity intensifies competitive adsorption of water molecules, both of which raise the baseline conductivity and its variance [13]. The multiplicative coupling of Φ with the node energy weight $S_{j,n}$ ensures that this environmental inflation is further modulated by the spectral content of each subband, so that low-energy high-frequency nodes, which are dominated by noise, are attenuated most aggressively, whereas high-energy approximation nodes carrying the true signal are largely preserved. This joint physical–statistical weighting is the principal reason the method sustains a low SNR variance across heterogeneous operating conditions.

The multiplicative synergy is also visible in the distribution of performance across experimental groups. Groups acquired near the environmental baseline (e.g., Group 8 at 25.00 °C and 37.73% RH) exhibit a comparatively smaller SNR improvement of 8.54 dB, because $\Phi \approx 1$ leaves the threshold nearly unadjusted and the algorithm behaves almost like a conventional soft-threshold WPD. In contrast, groups recorded further from the baseline (e.g., Group 11 at 39.68% RH and Group 17 at 41.74% RH) retain SNR improvements of 9.67 dB and 9.38 dB, respectively: performance degrades gracefully, rather than collapsing, as the operating point departs from the calibration conditions. This pattern corroborates the ablation results of Section 3.3, which shows that the environmental feedback contributes most precisely when it is most needed.

Relative to conventional single-threshold wavelet methods and to the moving-average and low-pass baselines, the proposed approach yields a consistent advantage across all 20 experimental groups rather than only under favorable conditions. Machine-learning-based denoising and drift-compensation schemes [19,20,39] can achieve comparable or superior accuracy but generally require substantial training data, offline model fitting, and

memory footprints that exceed the capacity of low-cost microcontrollers. Decomposition-based hybrids such as VMD- and EMD-assisted thresholding [27–29] incur iterative optimization that is difficult to bound within a fixed real-time budget. By contrast, the dual-feedback rule proposed here is a closed-form, single-pass operation whose cost scales linearly as O (N · J), making it well suited to embedded execution without sacrificing robustness. The measured latency of 1.4 ms per 256-sample frame and the 12 KB memory footprint confirm that the method is compatible with the timing and resource constraints of the STM32F103 platform, leaving ample headroom within the 1 s sampling interval for communication and housekeeping tasks [32,40]. This lightweight profile is particularly valuable for battery-powered or large-scale sensor deployments, where offloading denoising to the cloud would incur prohibitive energy and bandwidth costs [7,10]. Performing denoising at the perception layer also reduces the volume of data that must be transmitted upward through the four-layer architecture, improving end-to-end scalability and reducing the latency of cloud-side analytics.

To further situate the proposed method within the current denoising landscape, we qualitatively contextualize its performance against three additional families of state-of-the-art (SOTA) approaches. First, decomposition-based hybrids such as VMD–WPD [27] and EMD-assisted wavelet thresholding [28,29] have reported SNR improvements typically in the range of 8–12 dB on stationary or semi-stationary sensor signals. The proposed method achieves 9.86 dB in this same range while dispensing with the iterative mode-decomposition step, whose non-deterministic runtime is difficult to bound within the 1 s embedded budget of an STM32-class edge node. Second, spectral-graph wavelet thresholding [31] and data-driven optimal-basis selection [33] achieve competitive SNR but requires offline optimization on batch data and are not designed for per-frame streaming operation. Third, machine-learning-based drift compensation and denoising [19–21] can outperform classical methods when large, labeled datasets are available, but their memory footprints (typically hundreds of kilobytes to several megabytes) and inference latencies exceed the resources of the STM32F103C8T6 platform used in this work. A direct head-to-head benchmark against these SOTA methods would require re-implementing each on our exact hardware with independently tuned hyperparameters, which lies beyond the scope of the present study; we plan such a benchmark on a dedicated evaluation dataset in future work. The ablation study of Section 3.3 nevertheless provides component-level evidence that the observed performance gain originates specifically from the multiplicative dual-feedback rule, rather than from generic wavelet packet processing.

Although developed and validated for SGP30 MOX gas sensor signals, the proposed framework is not intrinsically gas specific. The wavelet packet front end, the MAD noise estimator, and the universal threshold operate on the statistical structure of the discrete-time signal alone and are therefore applicable, in principle, to any noisy sensor signal. Only the environmental feedback Φ encodes sensor-specific physics: for other MOX platforms (e.g., SGP40, BME680, CCS811 [17]) or for other sensor modalities, Φ must be reparameterized: specifically, the baseline point (T_0, H_0) and the sensitivity coefficients α and β must be recalibrated on the target device, whereas the multiplicative coupling rule and the node energy weighting remain unchanged. This separation between a signal-agnostic core and a small set of physically interpretable, recalibratable parameters is what makes the framework transferable.

Several limitations should be acknowledged. First, the experimental validation was conducted under controlled laboratory conditions over a moderate environmental range (24.09–26.00 °C and 34.09–45.02% RH); performance under rapidly changing or extreme environmental conditions requires further investigation, and the linear environmental correction of Equation (12) could be extended toward the full Arrhenius-type dependence

of Equation (10) to cover large deviations. Second, the sensitivity coefficients α and β were calibrated on a single sensor; unit-to-unit variability across a sensor population may require per-device recalibration. Third, the algorithm parameters are fixed offline; adaptive online estimation of the environmental coefficients, for example through recursive least squares, would allow the method to track sensor aging and seasonal drift. Further research directions include extension to multi-sensor arrays and integration of lightweight online machine learning techniques that preserve the real-time embedded profile [41,42].

5. Conclusions

This paper presents a novel wavelet packet decomposition-based denoising algorithm for SGP30 MOX gas sensor signals that integrates dynamic environmental physical feedback with adaptive node energy weights. The core innovation lies in the proposed dual-feedback adaptive threshold strategy, which combines physical environmental compensation (temperature–humidity correction factor) with statistical node energy weights through a multiplicative dual-feedback mechanism to achieve dynamic threshold adjustment. Through rigorous mathematical analysis and large-scale experimental validation encompassing 66,888 samples from 20 independent experimental groups, the following conclusions are drawn:

(1) The four-level sym5 wavelet packet decomposition, selected through Parseval energy conservation analysis and fifth-order Fourier polynomial fitting, provides optimal time–frequency resolution for SGP30 signals across 16 uniform subbands and achieves an SNR of 9.86 dB with an NMSE of 0.0009.

(2) The dual-feedback adaptive threshold, which multiplicatively couples the temperature–humidity correction factor with statistical node energy weights, achieves a weighted-average abnormal impulse suppression rate of 79.1%; the ablation study confirms that this multiplicative coupling is essential, outperforming the best single-feedback variant by 2.52 dB, whereas additive fusion yields no measurable gain over the feedback-free baseline.

(3) Controlled noise-injection validation against a fully known ground truth confirms an impulse suppression rate of 97.9–98.2% at impulse amplitudes up to $12\sigma_g$, compared with 29.7% and 61.1% for the hard- and soft-threshold baselines, and the embedded STM32F103 implementation executes in 1.4 ms per 256-sample frame with a memory footprint of about 12 KB, demonstrating practical feasibility for resource-constrained IoT monitoring.

The proposed method effectively enhances the monitoring sensitivity and reconstruction accuracy of low-cost gas sensors in complex dynamic environments, providing a reliable technical foundation for intelligent air quality monitoring systems.

Author Contributions: Conceptualization, X.F.; methodology, X.F. and L.X.; software, C.H. and H.G.; validation, C.H., L.N. and H.G.; formal analysis, L.X. and X.F.; investigation, C.H., H.G. and L.X.; resources, X.F. and L.X.; data curation, C.H. and H.G.; writing—original draft preparation, C.H. and X.F.; writing—review and editing, X.F., L.X. and L.N.; visualization, H.G. and C.H.; supervision, X.F.; project administration, X.F.; funding acquisition, X.F. All authors have read and agreed to the published version of the manuscript.

Funding: This research was funded by the National Key R&D Program of China, Intergovernmental International Science and Technology Innovation Cooperation Key Special Project ("International Science and Technology Innovation Cooperation between Governments—China–South Africa Special Project"): Research and Development of an Air–Space–Ground–Borehole Monitoring and Early-Warning Platform for the Water Environment of Deep Mineral Resource Mining Areas (Grant No. SQ2025YFE0106091); the Jianghuai Talent Program (Wan Zu Ban Zi [2025] No. 16); and the Guizhou Provincial Science and Technology Program, Guizhou Academician Workstation for Rich-Ore Fine Mining and Environmental Protection (Qian Ke He Pingtai KXJZ [2024]003).

Institutional Review Board Statement: Not applicable.

Informed Consent Statement: Not applicable.

Data Availability Statement: The data presented in this study are available upon request from the corresponding author. The data are not publicly available due to privacy restrictions.

Conflicts of Interest: The authors declare no conflicts of interest.

Abbreviations

The following abbreviations are used in this manuscript:

Abbreviation	Full Term
VOC	Volatile Organic Compound
MOX	Metal Oxide
TVOC	Total Volatile Organic Compound
eCO2	Equivalent Carbon Dioxide
IoT	Internet of Things
WT	Wavelet Transform
DWT	Discrete Wavelet Transform
WPD	Wavelet Packet Decomposition
SNR	Signal-to-Noise Ratio
NMSE	Normalized Mean Square Error
MA	Moving Average
LP	Low-Pass
IQR	Interquartile Range
MAD	Median Absolute Deviation

References

1. World Health Organization. *WHO Guidelines for Indoor Air Quality: Selected Pollutants*; WHO Regional Office for Europe: Geneva, Switzerland, 2010.
2. Kim, K.H.; Jahan, S.A.; Kabir, E.; Brown, R.J. A review of airborne polycyclic aromatic hydrocarbons (PAHs) and their human health effects. *Environ. Int.* **2013**, *60*, 71–80. [CrossRef] [PubMed]
3. Morati, N.; Contaret, T.; Gomri, S.; Fiorido, T.; Seguin, J.-L.; Bendahan, M. Noise spectroscopy data analysis-based gas identification with a single MOX sensor. *Sens. Actuators B Chem.* **2021**, *334*, 129654. [CrossRef]
4. Sensirion, A.G. *SGP30 Datasheet: Gas Sensor for Indoor Air Quality Applications*; Sensirion AG: Stäfa, Switzerland, 2018.
5. Yamazoe, N.; Shimanoe, K. New perspectives of gas sensor technology. *Sens. Actuators B Chem.* **2009**, *138*, 100–107. [CrossRef]
6. Abdullah, A.N.; Kamarudin, K.; Kamarudin, L.M.; Adom, A.H.; Mamduh, S.M.; Mohd Juffry, Z.H.; Bennetts, V.H. Correction model for metal oxide sensor drift caused by ambient temperature and humidity. *Sensors* **2022**, *22*, 3301. [CrossRef] [PubMed]
7. Ficili, I.; Giacobbe, M.; Tricomi, G.; Puliafito, A. From sensors to data intelligence: Leveraging IoT, cloud, and edge computing with AI. *Sensors* **2025**, *25*, 1763. [CrossRef] [PubMed]
8. Benammar, M.; Abdaoui, A.; Ahmad, S.H.M.; Touati, F.; Kadri, A. A modular IoT platform for real-time indoor air quality monitoring. *Sensors* **2018**, *18*, 581. [CrossRef] [PubMed]
9. Al-Okby, M.F.R.; Neubert, S.; Roddelkopf, T.; Fleischer, H.; Thurow, K. Evaluating IAQ-Index and TVOC parameter-based sensors for hazardous gases detection. *Sensors* **2022**, *22*, 1473. [CrossRef] [PubMed]
10. Neubert, S.; Roddelkopf, T.; Al-Okby, M.F.R.; Junginger, S.; Thurow, K. Flexible IoT gas sensor node for automated life science environments using stationary and mobile robots. *Sensors* **2021**, *21*, 7347. [CrossRef] [PubMed]
11. Jo, J.; Jo, B.W.; Kim, J.H.; Kim, S.J.; Han, W.Y. Development of an IoT-based indoor air quality monitoring platform. *J. Sens.* **2020**, *2020*, 8749764. [CrossRef]
12. Oh, J.; Kim, S.H.; Lee, M.-J.; Hwang, H.; Ku, W.; Lim, J.; Hwang, I.-S.; Lee, J.-H.; Hwang, J.-H. Machine learning-based discrimination of indoor pollutants using an oxide gas sensor array: High endurance against ambient humidity and temperature. *Sens. Actuators B Chem.* **2022**, *352*, 131894. [CrossRef]
13. Meng, F.; Ji, H.; Yuan, Z.; Chen, Y.; Zhang, H.; Qin, W. Dynamic measurement of VOCs with SnO_2 under temperature modulation. *IEEE Sens. J.* **2021**, *21*, 15889–15899. [CrossRef]
14. Nie, J.; Li, M.; Ji, H.; Li, G.; Li, Q.; Guo, C.; Meng, F. Humidity-conditioned drift compensation for temperature-modulated SnO_2 gas sensing for robust breath acetone quantification. *Sens. Actuators B Chem.* **2026**, *435*, 140157. [CrossRef]

15. Yang, W.; Li, W.; Lu, H.; Liu, J.; Zhang, T. Dynamic compensation method for humidity sensors based on temperature and humidity decoupling. *Sensors* **2022**, *22*, 7229. [CrossRef] [PubMed]
16. Tao, Y.; Xu, J.; Liang, Z.; Xiong, L.; Yang, H. Domain correction based on kernel transformation for drift compensation in E-nose. *Sensors* **2018**, *18*, 3209. [CrossRef] [PubMed]
17. Yurko, G.; Roostaei, J.; Dittrich, T.M.; Xu, L.; Ewing, M.; Zhang, Y.; Shreve, G. Real-time sensor response of 3 commercial MOX for BTEX detection. *Chemosensors* **2019**, *7*, 40. [CrossRef]
18. Zhang, W.; Yuan, Z.; Zhu, H.; Zhang, S.; Meng, F. Kinetic modeling in temperature-modulated semiconductor gas sensor. *ACS Sens.* **2024**, *9*, 4321–4330. [CrossRef] [PubMed]
19. Mei, H.; Peng, J.; Wang, T.; Zhang, B.; Xuan, F.; Wang, L.; Zeng, M.; Yang, Z. Smart VOCs recognition based on single gas sensor and multi-task deep learning. *Sens. Actuators B Chem.* **2025**, *433*, 137853. [CrossRef]
20. Zhang, T.; Tan, R.; Shen, W.; Lv, D.; Yin, J.; Chen, W.; Fu, H.; Song, W. Inkjet-printed ZnO MEMS sensor array for VOCs analysis. *Sens. Actuators B Chem.* **2023**, *393*, 133555. [CrossRef]
21. Khorramifar, A.; Karami, H.; Lvova, L.; Kolouri, A.; Lazuka, E.; Piłat-Rożek, M.; Lagod, G.; Ramos, J.A.; Lozano, J.; Kaveh, M.; et al. Environmental engineering applications of E-nose based on MOX. *Sensors* **2023**, *23*, 5716. [CrossRef] [PubMed]
22. Smith, S.W. *The Scientist and Engineer's Guide to Digital Signal Processing*; California Technical Publishing: San Diego, CA, USA, 1997.
23. Mallat, S. *A Wavelet Tour of Signal Processing*, 3rd ed.; Academic Press: San Diego, CA, USA, 2008.
24. Coifman, R.R.; Wickerhauser, M.V. Entropy-based algorithms for best basis selection. *IEEE Trans. Inf. Theory* **1992**, *38*, 713–718. [CrossRef]
25. Donoho, D.L.; Johnstone, J.M. Ideal spatial adaptation by wavelet shrinkage. *Biometrika* **1994**, *81*, 425–455. [CrossRef]
26. Donoho, D.L. De-noising by soft-thresholding. *IEEE Trans. Inf. Theory* **1995**, *41*, 613–627. [CrossRef]
27. Hou, C.; Yang, X.; Zhang, R.; Wang, J.; Shi, X.; Zhao, Z.; Wang, H. Novel denoising for wavelength modulation-direct absorption spectroscopy (WM-DAS) by variational mode decomposition (VMD) optimized by northern goshawk optimization (NGO) and wavelet packet decomposition (WPD). *Instrum. Sci. Technol.* **2026**, *54*, 287–301. [CrossRef]
28. Hu, H.; Ao, Y.; Yan, H.; Bai, Y.; Shi, N. Signal denoising based on wavelet threshold and optimized VMD. *J. Sens.* **2021**, *2021*, 5599096. [CrossRef]
29. Ch'ien, L.; Wang, Y.-j.; Shi, A.-c.; Wang, X.; Bai, J.; Wang, L.; Li, F. Noise suppression: EMD in NDIR gas detection systems. *Infrared Phys. Technol.* **2020**, *110*, 103335. [CrossRef]
30. Liu, Z.; Feng, X.; Dong, C.; Jiao, M. Denoising method of photoionization detector based on WPT. *Chemosensors* **2023**, *11*, 146. [CrossRef]
31. de Loynes, B.; Navarro, F.; Olivier, B. Data-driven thresholding in denoising with SGWT. *J. Comput. Appl. Math.* **2021**, *389*, 113319. [CrossRef]
32. Samann, F.; Bamerni, S.A.; Khorsheed, J.A.; Al-sulaifanie, A.K. Adaptive real-time wavelet denoising architecture based on feedback control loop. *J. Eng. Res.* **2021**, *9*, 1–18. [CrossRef]
33. Sahoo, G.R.; Freed, J.H.; Srivastava, M. Optimal wavelet selection for signal denoising. *IEEE Access* **2024**, *12*, 45369–45380. [CrossRef] [PubMed]
34. Rüffer, D.; Hoehne, F.; Bühler, J.; Bierer, B.; Wöllenstein, J.; Palzer, S. New digital metal-oxide (MOx) sensor platform. *Sensors* **2018**, *18*, 1052. [CrossRef] [PubMed]
35. Liu, H.; He, Y.; Nagashima, K.; Meng, G.; Dai, T.; Tong, B.; Deng, Z.; Wang, S.; Zhu, N.; Yanagida, T.; et al. Discrimination of VOCs via concealed features from temperature-modulated NiO sensor. *Sens. Actuators B Chem.* **2019**, *294*, 189–197. [CrossRef]
36. Daubechies, I. *Ten Lectures on Wavelets*; SIAM: Philadelphia, PA, USA, 1992.
37. ARM Ltd. CMSIS-DSP Software Library. Available online: https://www.keil.com/pack/doc/CMSIS/DSP/html/index.html (accessed on 2 September 2026).
38. Shin, W.; Hong, S.; Jeong, Y.; Jung, G.; Park, J.; Kim, D.; Choi, K.; Shin, H.; Koo, R.-H.; Kim, J.-J.; et al. Low-frequency noise in gas sensors: A review. *Sens. Actuators B Chem.* **2023**, *393*, 133551. [CrossRef]
39. Li, R.; Li, Z.; Kofi, B.A.; Sun, J.; He, Y.; Jiao, M. A Comprehensive Review of Algorithms for Drift Compensation in Metal Oxide Semiconductor Gas Sensor Arrays. *Chemosensors* **2026**, *14*, 143. [CrossRef]
40. Liu, B.; Zhou, Y.; Fu, H.; Fu, P.; Feng, L. Lightweight self-detection and self-calibration for MEMS gas arrays. *Sensors* **2022**, *22*, 4315. [CrossRef] [PubMed]
41. Jung, H.T. The present and future of gas sensors. *ACS Sens.* **2022**, *7*, 912–913. [CrossRef] [PubMed]
42. Cheng, L.; Meng, Q.-H.; Lilienthal, A.J.; Qi, P.-F. Development of compact electronic noses: A review. *Meas. Sci. Technol.* **2021**, *32*, 062002. [CrossRef]

Disclaimer/Publisher's Note: The statements, opinions and data contained in all publications are solely those of the individual author(s) and contributor(s) and not of MDPI and/or the editor(s). MDPI and/or the editor(s) disclaim responsibility for any injury to people or property resulting from any ideas, methods, instructions or products referred to in the content.